

Spatial characterization of Fraunhofer diffraction in a four-level light-matter-coupling systemSeyyed Hossein Asadpour ¹, Teodora Kirova ^{2,*}, Hamid R. Hamedi ³ and Reza Asgari ^{1,†}¹*School of Physics, Institute for Research in Fundamental Sciences, IPM, Tehran, 19395-5531, Iran*²*Institute of Atomic Physics and Spectroscopy, University of Latvia, LV-1004, Latvia*³*Institute of Theoretical Physics and Astronomy, Vilnius University, LT-10257, Lithuania*

(Received 17 August 2023; revised 17 November 2023; accepted 8 January 2024; published 6 February 2024)

We explore the spatial features of various orders of Fraunhofer diffraction patterns in a four-level N -type atomic system. The system interacts with a weak probe light, a standing wave (SW) coupling field in the x direction, and a cylindrical beam of composite optical vortex type. We derive the first-order linear and third-order cross-Kerr nonlinear parts of the probe susceptibility by expanding the probe susceptibility of the system into the second order of the SW beam. This allows us to solve the integral equation of Fraunhofer diffraction, decoding its varying degrees to specific degrees of Bessel functions containing the nonlinear susceptibility. Notably, the nonlinear susceptibility exhibits dependence on the orbital angular momentum (OAM) of the light beam, leading to spatial variations in the Bessel functions, and consequently, in the different orders of Fraunhofer diffraction. Leveraging the manipulation of OAM, we achieve precise control over the spatial mapping of diverse diffraction orders at various locations. Our research sheds light on the spatial behavior of Fraunhofer diffraction in complex atomic systems. It presents exciting prospects for harnessing the OAM characteristics of light in future optical technologies.

DOI: [10.1103/PhysRevA.109.023702](https://doi.org/10.1103/PhysRevA.109.023702)**I. INTRODUCTION**

Electromagnetically induced grating (EIG) is a fascinating phenomenon that occurs in atomic systems under the influence of laser fields. The concept of EIG [1–3] comes to the forefront when the conventional traveling wave (TW) coupling field, commonly observed in electromagnetically induced transparency (EIT) systems [4–7], is substituted with a standing-wave (SW) coupling beam. Upon introducing the SW control field, an intriguing spatial periodicity emerges in the absorption and dispersion characteristics of the TW probe beam, leading to the deflection of the probe field into high-order directions. These unique EIG properties have significant implications for various applications in the field of optics and open up new perspectives on the interplay between light and matter and pave the way for the creation of optical systems and devices of the utmost quality. They find use in optical switching [8,9], storage of light [10], all-optical beam splitting and fanning [11], as well as novel implementations in electromagnetically induced Talbot effect [12], optical bistabilities [13], topological insulators [14], and soliton physics [15,16], to name a few.

Current studies on the EIG have surpassed the traditional Λ configuration and expanded to encompass interactions of many-level schemes with multiple beams, such as Ξ -type [17] and Y -type excitations [18], tripod systems [19], and other four-level arrangements [20]. Furthermore, EIG effects have been successfully extended to various media, moving beyond

the initial observations in hot and ultracold atoms. Notably, researchers have explored EIG in quantum dot molecules [21–23], showcasing its applicability in more complex systems. Additionally, we recently described EIG in the vicinity of a plasmonic nanostructure in our works [24,25], highlighting its potential in novel applications involving plasmonics.

As emphasized in [26], the interaction of the EIG systems with optical vortex beams, i.e., light beams carrying orbital angular momentum (OAM) [27–29], is especially beneficial in terms of providing new degrees of freedom for manipulating the performance of the optical grating. In particular, it has been shown that by varying the winding number of the vortex beam, one can achieve direct control of the transfer of the probe beam energy from the zero- to high-diffraction orders [26].

The interaction of Laguerre-Gaussian (LG) beams with atomic systems represents a well-established and thriving direction in optical physics, leading to an increasing number of significant applications [30–33]. These applications span across diverse fields, including interdisciplinary studies [34,35], further amplifying the impact of this research area.

Remarkably, recent advancements in experimental techniques have enabled the realization of optical vortex fields in various forms and complexities. Researchers can now engineer these fields with specific OAM, polarization, and in different geometrical arrangements.

Of particular interest to our research is the interaction of EIGs with composite optical vortices, which result from the interference of two or more vortex beams [36]. Under certain conditions for the OAMs, intriguing “petals”-like periodic intensity structures can be observed [37,38]. The ability to control the diffraction intensity distribution of the probe

*teo@lu.lv

†asgari@ipm.ir

field to different locations in a two-dimensional (2D) EIG by manipulating the OAM of the composite vortex beam was demonstrated in [39]. This showcases the potential of tailored optical vortices in directing and shaping EIGs for desired applications. Similarly, analogous effects were observed in a 2D EIG system utilizing a tripod configuration of atomic levels [40]. These results highlight the adaptability and importance of investigating composite optical vortices in EIG studies, where the exact regulation of light-matter interactions holds promise for a variety of prospective applications.

EIGs also play a significant role in the generation of holographic gratings and optical modes. In a recent study by Arkhipkin *et al.* [41], the Fresnel diffraction of optical vortex light within a Raman interaction atomic medium with a spatially periodic pump field was investigated. Under specific conditions and at distances corresponding to classical Talbot planes, the study revealed the emergence of periodic amplitude-phase distributions. Another investigation [42] focused on the near-field diffraction of optical vortex light on a fork-shaped grating with different topological charges. This study explored the evolution of specific optical vortices during propagation.

Among other novel applications of composite Laguerre-Gaussian beams are bright or dark ring lattices for trapping atoms [43,44], including the creation of artificial gauge magnetic and electric fields [45], as well as more exotic phenomena, such as applications as wave-front sensors [46], or the so-called azimuths [47,48], which represent a special class of spatially localized self-trapped ringlike beams.

In this current study, we expand upon our previous research [39], focusing on investigating the spatially dependent diffraction efficiencies of an N -type four-level EIG scheme interacting with composite vortex light. For this purpose, we employ two spatially dependent coupling fields, a SW in the x direction, and a composite vortex beam, both simultaneously interacting with the atomic energy levels. Expanding the steady-state probe susceptibility to the second order with respect to the SW beam allows us to uncover the contributions of its first-order linear effect and third-order cross-Kerr nonlinear effect. To analyze the resulting diffraction pattern, by employing analytical methods, we solve the integral equation of Fraunhofer diffraction. This solution reveals a dependence on Bessel functions that incorporate the nonlinear susceptibility. As the nonlinear susceptibility is contingent on the topological charge of the composite beam, it introduces spatial variations in the Bessel functions, and hence, subsequently, on different orders of Fraunhofer diffraction.

In our numerical calculations, we first consider the cases of a simple vortex field, as well as a composite vortex with different winding numbers, subsequently we focus on the situation when a composite vortex beam with the same OAM numbers is applied with two specific cases for the detunings of the three laser fields interacting with the atomic transitions. Through these calculations, we demonstrate that the intensity pattern of the probe field diffraction exhibits spatial distribution at different locations, which can be effectively controlled by simply adjusting the OAM values of the composite vortex field. For zero values of the winding number, the diffraction of the zeroth, first, and second orders display distinct ring patterns with varying intensities, arising from destructive and

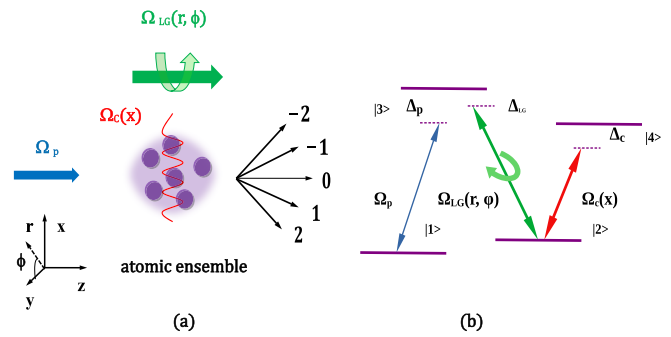


FIG. 1. (a) Excitation scheme of atomic ensemble in EIG. (b) Proposed four-level N -type excitation scheme, with two ground states denoted as $|1\rangle$ and $|2\rangle$, along with two excited states represented by $|3\rangle$ and $|4\rangle$. These energy levels interact with three lasers: a weak TW probe field with Rabi frequency Ω_p , a strong SW field with Rabi frequency $\Omega_c(x)$, and a Laguerre-Gaussian beam with Rabi frequency denoted as $\Omega_{LG}(r, \phi)$.

constructive interference. When the OAM is nonzero, these ring shapes transform into intriguing petal-like structures, diminishing in size as the diffraction order grows. In addition, we study the behavior of the different orders of Fraunhofer diffraction patterns versus the atomic interaction length for different OAM numbers, showing how the energy of the probe field is distributed.

The simplicity and effectiveness of this proposed scheme for controlling diffraction intensity make it particularly appealing for future experimental realizations and applications. It offers a mechanism to customise and manipulate light-matter interactions to suit particular applications in optical technologies, which has significant potential for creating photonic components and systems that take advantage of the OAM of light.

The paper is organized along the following lines. After an Introduction, in Sec. II we develop the groundwork of our theoretical model for the planned numerical calculations. Employing Maxwell's equation in the slowly varying envelope approximation in the steady-state regime, as well as the Fraunhofer diffraction equation, in Sec. III we proceed to derive the analytical expressions for the spatial diffraction intensities of the zero, first, and second orders. Section IV is devoted to the analysis of the obtained numerical results of the spatial diffraction intensities, including a variation of different system parameters, such as laser beam detunings and field strengths, atomic interaction length, as well as OAM numbers of the same or different values of the composite vortex beam. In Sec. V we recap the main results, in parallel giving directions for future experimental realizations and feasible applications of our studies.

II. MODEL AND THEORY

The system of interest consists of in a four-level N -type atomic configuration with two ground states $|1\rangle$, $|2\rangle$ and two excited states $|3\rangle$, $|4\rangle$ as shown in Fig. 1. The atomic levels in our system are coupled by three laser fields. The first laser is a weak light with a Rabi frequency of Ω_p , which specifically probes the $|1\rangle \rightarrow |3\rangle$ transition. The transition

$|2\rangle \rightarrow |4\rangle$ is derived with a coupling field with Rabi frequency of Ω_c . Finally, a third laser beam, denoted as Ω_{LG} interacts with the $|2\rangle \rightarrow |3\rangle$ transition. The Rabi-frequencies of probe and coupling fields are defined as $\Omega_p = \vec{\mu}_{13} \cdot \vec{E}_p/2\hbar$, $\Omega_c = \vec{\mu}_{24} \cdot \vec{E}_c/2\hbar$, and $\Omega_{LG} = \vec{\mu}_{23} \cdot \vec{E}_{LG}/2\hbar$, with $\vec{\mu}_{ij}$ being the electric-dipole transition matrix element of $|i\rangle \rightarrow |j\rangle$.

We adopt the interaction picture, employing the electric dipole and rotating wave approximations. Under these assumptions, the total Hamiltonian of the system can be expressed as follows:

$$H_{\text{int}} = -\hbar(\Delta_p - \Delta_{LG})|2\rangle\langle 2| - \hbar\Delta_p|3\rangle\langle 3| \\ - \hbar(\Delta_p - \Delta_{LG} + \Delta_c)|4\rangle\langle 4| \\ - \hbar(\Omega_p|3\rangle\langle 1| + \Omega_{LG}|3\rangle\langle 2| + \Omega_c|4\rangle\langle 2| + \text{H.c.}). \quad (1)$$

In the above, we define the laser detunings as $\Delta_p = \omega_p - \omega_{31}$, $\Delta_c = \omega_c - \omega_{42}$, and $\Delta_{LG} = \omega_{LG} - \omega_{32}$, where ω_p , ω_c , ω_{LG} are the laser beams' frequencies, and ω_{ij} , ($i, j = 1..4$) are the resonant frequencies of the corresponding atomic transitions $|i\rangle \rightarrow |j\rangle$.

The wave function of the system is decomposed into the basis set of atomic levels; $\{|1\rangle, |2\rangle, |3\rangle, |4\rangle\}$, i.e., $\Psi(t) = \sum_{i=1,4} a_i(t)e^{-i\omega_i t}|i\rangle$, involving the time-dependent coefficients $a_i(t)$, as well as the atomic levels energies $\hbar\omega_i$, ($i = 1, \dots, 4$). The dynamics of the system are described by the equations of motion for the probability amplitudes of all atomic states

$$\frac{da_1}{dt} = i\Omega_p a_3, \\ \frac{da_2}{dt} = i[(\Delta_p - \Delta_{LG})a_2 + \Omega_{LG}a_3 + \Omega_c a_4] - \gamma_2 a_2, \\ \frac{da_3}{dt} = i(\Omega_p a_1 + \Omega_{LG}a_2 + \Delta_p a_3) - \frac{\Gamma_3}{2} a_3, \\ \frac{da_4}{dt} = i[\Omega_c a_2 + (\Delta_p - \Delta_{LG} + \Delta_c)a_4] - \frac{\Gamma_4}{2} a_4. \quad (2)$$

The parameters Γ_3 , Γ_4 , and γ_2 indicate the decay rates from the upper levels $|3\rangle$, and $|4\rangle$, as well as the ground state decoherence, respectively. In what follows, we will assume $\Gamma_3 = \Gamma_4 = \gamma$ and express all other parameters in units of γ .

Under the weak probe-field approximation, specifically when $|a_1|^2 \approx 1$, the susceptibility of the probe field can be derived by solving Eqs. (2) under the steady-state condition as follows:

$$\chi_p = \frac{N\mu_{13}^2}{2\varepsilon_0\hbar} \chi(\omega_p). \quad (3)$$

We use the definition of the polarization of the medium $\vec{P}_p = N\vec{\mu}_{13}a_3a_1^*$ where N shows the atomic density, and ε_0 is the dielectric constant in a vacuum. The form of $\chi(\omega_p)$ is given by

$$\chi(\omega_p) = \frac{A_2A_4 - \Omega_c^2}{A_4(A_2A_3 - \Omega_{LG}^2) - A_3\Omega_c^2}, \quad (4)$$

where, for the sake of simplicity, we introduce the following notations:

$$A_2 = \Delta_p - \Delta_{LG} + i\gamma_2; \quad A_3 = \Delta_p + i\frac{\Gamma_3}{2}; \\ A_4 = \Delta_p - \Delta_{LG} + \Delta_c + i\frac{\Gamma_4}{2}. \quad (5)$$

To analyze the nonlinear modulation induced by the control field with SW pattern, we expand $\chi(\omega_p)$ into the second order of Ω_c as

$$\chi(\omega_p) = \chi^{(1)}(\omega_p) + \Omega_c^2 \chi^{(3)}(\omega_p). \quad (6)$$

The first- and third-order Kerr nonlinear parts of the probe susceptibility are then given by

$$\chi^{(1)}(\omega_p) = -\frac{A_3}{A_2A_3 - \Omega_{LG}^2(r, \varphi)}, \quad (7)$$

$$\chi^{(3)}(\omega_p) = -\frac{\Omega_{LG}^2(r, \varphi)}{A_4|A_2A_3 - \Omega_{LG}^2(r, \varphi)|^2}. \quad (8)$$

Control fields that have SW patterns, in turn, cause spatial modulation of the probe beam absorption and refraction. As a consequence of the intensity-dependent susceptibility, the atomic system acts as a grating, diffracting the probe beam in different directions.

For the purposes of observing these effects, we will then utilize a coupling field $\Omega_c = \Omega_{c0}[\sin(\pi x/\Lambda_x)]$, which constitutes a SW with a space frequency Λ_x along the x direction. Moreover, we replace the Ω_{LG} field with a composite vortex beam, i.e., a superposition of two vortices

$$\Omega_{LG} = \Omega e^{-r^2/w^2} [(r/w)^{|l_1|} e^{il_1\varphi} + (r/w)^{|l_2|} e^{il_2\varphi}], \quad (9)$$

where w is the beam waist and its value is in order of μm , the radial distance from the axis of the LG beam is represented by $r = \sqrt{x_1^2 + y_1^2}$, with l_1, l_2 providing the winding numbers, and φ is the azimuthal angle. We can simplify the expressions by assuming $l_1 = -l_2 = l$:

$$\Omega_{LG} = \Omega_{lg} \cos(l\varphi); \quad \Omega_{lg} = 2\Omega e^{-r^2/w^2} (r/w)^{|l|}. \quad (10)$$

III. FRAUNHOFER DIFFRACTION PATTERN

By employing Maxwell's equations in the slowly varying envelope approximation and considering the steady-state regime, we can derive the diffraction pattern of the probe beam as follows:

$$\frac{\partial E_p}{\partial z} = i\frac{\pi}{\varepsilon_0\lambda_p} P_p, \quad P_p = \varepsilon_0 \chi(\omega_p) E_p, \quad (11)$$

with λ_p denoting the probe light wavelength. The above can be rewritten as

$$\frac{\partial E_p}{\partial z'} = i\gamma \chi(\omega_p) E_p, \quad (12)$$

where we introduced the definition $z' = (\pi N\mu_{13}^2)/(\hbar\varepsilon_0\lambda_p\gamma)z$. In what follows we will work with a dimensionless z' , by treating $\xi = (\hbar\varepsilon_0\lambda_p\gamma)/(\pi N\mu_{13}^2)$ as the unit for z . The parameter ξ can be controlled by the atomic density of the medium, and its order is about μm .

The transmission function of the grating is determined by

$$T(x) = e^{-\text{Im}[\chi(\omega_p)]L} e^{i\text{Re}[\chi(\omega_p)]L}, \quad (13)$$

where L is the interaction length. The first and second exponential terms correspond to the grating amplitude and phase modulation, respectively. After performing the Fourier transforming of Eq. (13), we arrive at the expression for Fraunhofer diffraction

$$I_p(\theta_x) = |E(\theta_x)|^2 \frac{\sin^2(M\pi \Lambda_x \sin \theta_x / \lambda_p)}{M^2 \sin^2(\pi \Lambda_x \sin \theta_x / \lambda_p)}, \quad (14)$$

where

$$E(\theta_x) = \int_0^1 T(x) \exp(-i2\pi x \Lambda_x \sin \theta_x / \lambda_p) dx. \quad (15)$$

The m th-order diffraction angle θ_x with respect to the z direction is calculated from $\sin \theta_x = m\lambda_p / \Lambda_x$.

We are interested in investigating the Fraunhofer diffraction orders by analytically solving Eq. (15). For this purpose, we need to solve Eq. (13) first. By inserting Eq. (6) in Eq. (13) the transmission function of the 2D grating is given by

$$T(x) = e^{-\text{Im}[\chi^{(1)}(\omega_p) + \Omega_c^2 \chi^{(3)}(\omega_p)]L} e^{i\text{Re}[\chi^{(1)}(\omega_p) + \Omega_c^2 \chi^{(3)}(\omega_p)]L}. \quad (16)$$

It should be reminded that $\Omega_c^2(x) = \Omega_{c0}^2 \sin^2(\pi x / \Lambda_x)$. By presenting $\chi^{(3)}(\omega_p)$ in the form of $\chi^{(3)}(\omega_p) = A + iB$; $\text{Re}[\chi^{(3)}(\omega_p)] = A$; $\text{Im}[\chi^{(3)}(\omega_p)] = B$, and using a new notation $k = \exp(\{-\text{Im}[\chi^{(1)}(\omega_p)] + i\text{Re}[\chi^{(1)}(\omega_p)]\}L)$, we get a new expression of Eq. (15):

$$E(\theta_x) = k \int_0^1 \exp[iL\chi^{(3)}(\omega_p)\Omega_{c0}^2 \sin^2(\pi x / \Lambda_x)] \times \exp(-i2\pi x \Lambda_x \sin \theta_x / \lambda_p) dx. \quad (17)$$

By setting $M = L\chi^{(3)}(\omega_p)\Omega_{c0}^2$ in Eq. (17) we obtain

$$E(\theta_x) = k \exp\left(\frac{iM}{2}\right) \int_0^1 \exp\left(-i\frac{M}{2} \cos(2\pi x / \Lambda_x)\right) \times \exp(-i2\pi x \Lambda_x \sin \theta_x / \lambda_p) dx. \quad (18)$$

To further simplify the above expression we introduce $\phi = \frac{2\pi x}{\Lambda_x}$ and $n = \Lambda_x \sin \theta_x / \lambda_p$ and arrive at

$$E(\theta_x) = k \exp\left(\frac{iM}{2}\right) \int_0^{2\pi} \exp\left(-i\frac{M}{2} \cos \phi\right) \times \exp(-in\phi) \left(\frac{\Lambda_x}{2\pi}\right) d\phi. \quad (19)$$

Next, we define $M' = -M/2$ and $P = k \exp\left(\frac{iM}{2}\right) \left(\frac{\Lambda_x}{2\pi}\right)$, and we use the following integral:

$$\int_0^{2\pi} \exp[-i(n\phi - M' \cos \phi)] d\phi = \int_0^{2\pi} [\cos(n\phi - M' \cos \phi) - i \sin(n\phi - M' \cos \phi)] d\phi. \quad (20)$$

Since the first term of Eq. (20) gives zero, Eq. (19) attains a simplified form

$$E(\theta_x) = -iP \int_0^{2\pi} \sin(n\phi - M' \cos \phi) d\phi = iP2\pi J_n(M'), \quad (21)$$

where $J_n(M')$ represents a Bessel function of the n th order. Plugging the definitions of P , M' , and further k , M into Eq. (21), renders the final expression for $E(\theta_x)$:

$$E(\theta_x) = -i\Lambda_x \exp\left\{iL\left[\chi^{(1)}(\omega_p) + \frac{1}{2}\chi^{(3)}(\omega_p)\Omega_{c0}^2\right]\right\} \times J_n\left(-\frac{L\chi^{(3)}(\omega_p)\Omega_{c0}^2}{2}\right). \quad (22)$$

We can now proceed to obtain the n -order diffraction intensity by combining Eqs. (15) and (22)

$$I(\theta_x^{(n)}) = \left|\Pi J_n\left(-\frac{L\chi^{(3)}(\omega_p)\Omega_{c0}^2}{2}\right)\right|^2. \quad (23)$$

Here Π stands for the following expression:

$$\Pi = -i\Lambda_x \exp\left\{iL\left[\chi^{(1)}(\omega_p) + \frac{1}{2}\chi^{(3)}(\omega_p)\Omega_{c0}^2\right]\right\}. \quad (24)$$

In the following discussion, we mainly concentrate on the spatial diffraction intensities of the zero, first, and second orders as follows:

$$\begin{aligned} I(\theta_x^{(0)}) &= \left|\Pi J_0\left(-\frac{L\chi^{(3)}(\omega_p)\Omega_{c0}^2}{2}\right)\right|^2, \\ I(\theta_x^{(1)}) &= \left|\Pi J_1\left(-\frac{L\chi^{(3)}(\omega_p)\Omega_{c0}^2}{2}\right)\right|^2, \\ I(\theta_x^{(2)}) &= \left|\Pi J_2\left(-\frac{L\chi^{(3)}(\omega_p)\Omega_{c0}^2}{2}\right)\right|^2. \end{aligned} \quad (25)$$

It is clear from expressions in Eq. (25) that the different orders of the Fraunhofer diffraction are directly related to the identical orders of the Bessel function.

IV. RESULTS AND DISCUSSIONS

In this section, we will discuss the spatial dependency of the different orders of the grating by adjusting the OAM of the composite vortex light l in cases of different detunings of the three laser fields interacting with the N -type atomic system. We will also investigate how the different orders of Fraunhofer diffraction behave, i.e., what is the distribution of probe field energy, as a function of the atomic interaction length for different winding numbers of the composite vortex beam.

A. Case of simple vortex field

To begin with a simpler scenario, let us consider the setup where a basic vortex beam is employed. In Fig. 2, we display the different orders of the Fraunhofer diffraction pattern versus the detunings of the coupling fields Δ_c and Δ_{LG} when the probe light is in resonance with its transition (i.e., $\Delta_p = 0$). As seen here, the intensity of the different orders can be controlled by the detunings of the coupling lights. When the coupling lights are off-resonate, more of the probe energy gathers in the first order ($-1 \leq \Delta_c \leq -2$; $-1 \leq \Delta_{LG} \leq -2$) and ($1 \leq \Delta_c \leq 2$; $1 \leq \Delta_{LG} \leq 2$). In other similar regimes for the detunings (indicated by the yellow band in the higher orders) the intensity of the diffraction orders may be higher than the zero order.

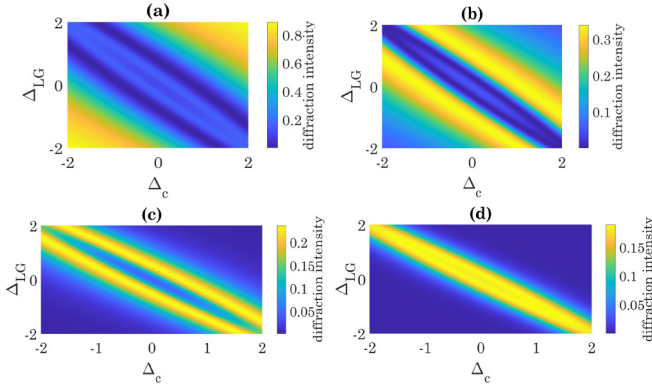


FIG. 2. Different orders of the Fraunhofer diffraction pattern versus the parameters Δ_c and Δ_{LG} . Panel (a) corresponds to the zero order, (b) corresponds to the first order, (c) corresponds to the second order, and (d) corresponds to the third order. The selected parameters are $\Delta_p = 0$, $\Omega_{c0} = 0.5\gamma$, $\Omega = 1.5\gamma$, $L/\xi = 50$.

B. Case of composite vortex with different OAMs

As a second step we apply the composite form of the optical vortex light [Eq. (9)] considering different values of the winding numbers l_1 and l_2 . As shown in Fig. 3, we present the Fraunhofer diffraction patterns for this composite beam with $l_1 = 4$ and $l_2 = -1$. The results in Fig. 3 are decomposed into different parts to visualize the various diffraction orders. Figures 3(a), 3(b), 3(c), and 3(d) correspond to the zero order, the first order, the second order, and the third order, respectively. This comprehensive representation of the different diffraction orders provides a more complete and detailed view of the pattern for the composite beam.

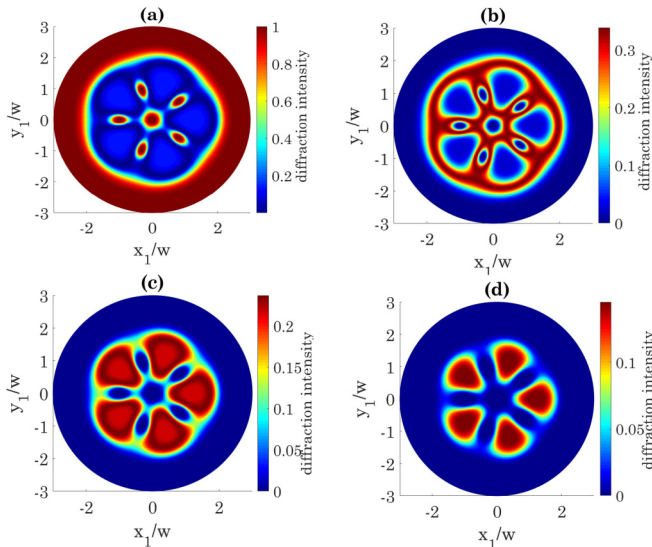


FIG. 3. Spatial dependency of the different diffraction orders versus x_1/w and y_1/w for $l_1 = 4$ and $l_2 = -1$. Panel (a) corresponds to the zero order, (b) corresponds to the first order, (c) corresponds to the second order, and (d) corresponds to the third order. The selected parameters are $\Delta_p = 0$, $\Delta_c = -1$, $\Delta_{LG} = 2$, $\Omega_{c0} = 0.5\gamma$, $\Omega = 1.1\gamma$, $L/\xi = 50$.

As discussed in [31], a composite twisted beam with different values of l_1 and l_2 exhibits a central vortex of charge l_1 , surrounded by $|l_1 - l_2|$ peripheral vortices. Our findings concerning the diffraction patterns and the spatial mapping of different orders strongly align with the structural characteristics of such a composite vortex. Specifically, we observe that the different diffraction orders of the grating exhibit a prominent five-fold symmetry, which directly corresponds to the presence of $|l_1 - l_2|$ peripheral vortices in the composite beam. For the zero-order grating [Fig. 3(a)], the majority of light is concentrated at the core of the azimuthal space, consistent with the central vortex of the composite beam. Furthermore, the zero-order grating exhibits five peripheral spots precisely located at the positions where the singularity points of the peripheral vortices in the composite beam are situated. Surrounding this central region, there is a ring-shaped area where the probe field energy is entirely reconstituted.

In contrast, the first-order grating illustrated in Fig. 3(b) produces a distinctive wheel-like pattern, indicating a significant change in energy distribution compared to the zero order. In this case, the energy is concentrated in locations that were previously completely devoid of it, essentially creating an antiphase relationship with the zero order. With the higher second- [Fig. 3(c)] and third- [Fig. 3(d)] orders of grating, the patterns undergo structural changes while still retaining the five-fold symmetry.

C. Case of composite vortex with same OAMs

As mentioned in Sec. II, the main focus of our investigations is the case of equal winding numbers $l_1 = l_2$ of the composite vortex coupling field [see Eq. (10)].

1. Resonant probe and coupling fields

We first investigate the case when all laser beams are resonant with the respective atomic transitions, e.g., $\Delta_p = \Delta_c = \Delta_{LG} = 0$. In Fig. 4, we present the spatial properties of the different orders of diffraction patterns for a winding number $l = 0$. The blue areas indicate regions of low intensity in the diffraction pattern, while the dark red structures represent positions of high-intensity diffraction. When $l = 0$, the diffraction intensities of the zero [Fig. 4(a)], first [Fig. 4(b)], and second [Fig. 4(c)] orders exhibit distinct ring patterns. For the zero order, the majority of the energy is concentrated at the center, forming a high-intensity region surrounded by a ring-shaped area where the probe-field energy is completely absent. This ring-shaped void represents a region of destructive interference, arising from the diffraction process. Moving away from this zero-energy ring, the energy starts to reappear. In contrast, for the first and second orders of diffraction, the energy distribution undergoes a fascinating transformation. In these cases, the central region experiences a complete absence of energy, resulting in a dark spot at the center. As one moves away from the center, the energy becomes manifest, taking the form of a ring, indicating its presence. This ring-shaped region represents constructive interference, where the diffracted waves combine to create regions of increased intensity. As the order of the grating increases, the ring patterns gradually shrink and narrow. This reduction in size and width of the grating rings is a consequence of the increasing complexity of

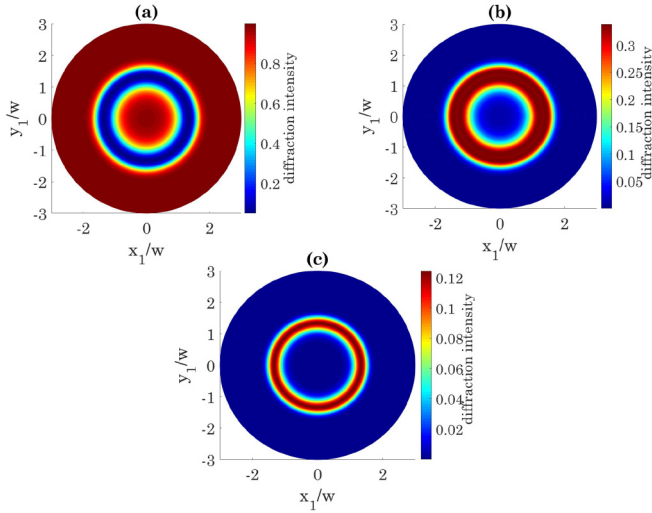


FIG. 4. Spatial dependency of the different diffraction orders versus x_1/w and y_1/w for winding number $l = 0$. Panel (a) corresponds to the zero order, (b) corresponds to the first order, and (c) corresponds to the second order. The selected parameters are $\Delta_p = \Delta_c = \Delta_{LG} = 0$, $\Omega_{c0} = 0.2\gamma$, $\Omega = 1.5\gamma$, $L/\xi = 50$. Notice that, for the first and second orders of diffraction, the energy distribution undergoes a pattern in which the central region experiences a complete absence of energy, resulting in a dark spot at the center.

the diffraction process, leading to more intricate interference patterns. In higher-order diffraction patterns, the ring-shaped regions become progressively smaller and tighter, reflecting the rich and intricate behavior of the diffraction process. Consequently, the number and intensity of these bright and dark regions depend on the size and microscopic structure of the atoms and the wavelength of the incident light.

Further, Fig. 5 shows the diffraction patterns and the spatial mapping of the various orders when $l = 2$. Here, we observe a petal-like pattern for the different diffraction orders. Figures 5(a) to 5(c) provide a visual representation of the diffracted patterns observed for the zero to second orders of diffraction. These figures reveal intriguing characteristics exhibited by gratings of different orders. Notably, each order of the grating displays a distinctive pattern with a symmetrical arrangement resembling petals. Upon closer examination, it becomes apparent that the light distribution within the azimuthal space differs, depending on the diffraction order. In the case of zero order, the light is predominantly concentrated at the center, forming an intriguing anti-petal-like pattern. The energy of the diffracted light appears to converge towards the central region, resulting in reduced intensity towards the outer areas. However, as we move to higher orders of diffraction such as the first and second orders, the dynamics of light distribution undergoes a remarkable change. In these instances, the light is no longer focused at the center but gathers primarily at the petal regions. The central region, which was previously the focal point of energy, now experiences a complete absence of light. This unique behavior of light distribution creates a distinctive pattern with zero intensity at the center and enhanced intensity at the petals. Furthermore, as the order of diffraction increases, the petal patterns gradually diminish in size. This is clearly illustrated in Fig. 5(c), where

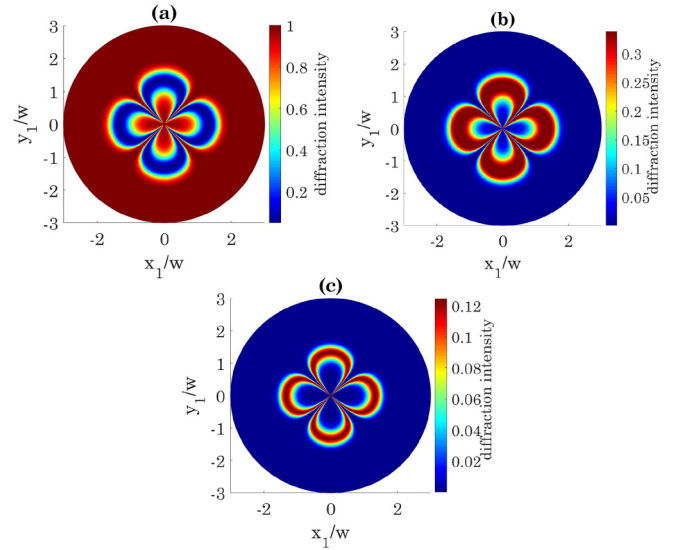


FIG. 5. Spatial dependency of the different diffraction orders versus x_1/w and y_1/w for winding number $l = 2$. Panel (a) corresponds to the zero order, (b) corresponds to the first order, and (c) corresponds to the second order. The light distribution within the azimuthal space differs, depending on the diffraction order. The selected parameters are the same as in Fig. 4.

the petals become smaller and more compact, compared to the lower orders. The shrinking of the petal patterns with increasing order highlights the intricate relationship between diffraction and the resulting spatial distribution of light.

2. Resonant probe and off-resonant coupling fields

In what follows, we will study the azimuthal dependence of the different diffraction orders in the off-resonance conditions for the coupling and composite optical vortex lights, while the probe field is still resonant, i.e., $\Delta_p = 0$, $\Delta_c = -\gamma$, $\Delta_{LG} = 2\gamma$.

The numerical results for the case of winding number $l = 0$ are given in Fig. 6. In this analysis, it is evident that the distribution of intensity in the zero order [Fig. 6(a)] attains its maximum value in regions that are situated away from the center. At the same time, the distribution of intensities experiences a lower value in the central regions. In the case of the first order [Fig. 6(b)], the intensity distribution reaches its maximum value at the center and gradually decreases in regions distant from the center. The second order [Fig. 6(c)] reveals that the intensity distribution is visible in the central regions, but its value is comparably lower than that of the zero and first orders. Nevertheless, in some narrow regions of space, the distribution of intensity surpasses the zero and first orders. As for the third order, shown in Fig. 6(d), we observe that there is no intensity distribution in both the central and outer regions, with only a few areas exhibiting a weak intensity distribution, which is inferior to that of other orders.

Furthermore, we explore the behavior of the grating for the nonzero OAM number $l = 2$, as depicted in Fig. 7. The intensity distribution exhibits petal-like patterns for different degrees of diffraction. Notably, the probe field's highest-energy concentration occurs in the first-order [Fig. 7(b)]

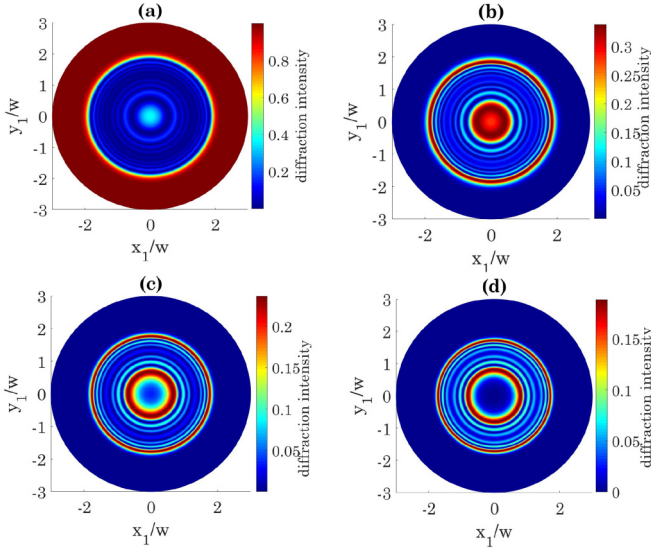


FIG. 6. Spatial dependency of the different diffraction orders versus x_1/w and y_1/w for winding number $l = 0$. Panel (a) corresponds to the zero order, (b) corresponds to the first order, (c) corresponds to the second order, and (d) corresponds to the third order. The selected parameters are $\Delta_c = -\gamma$, $\Delta_{LG} = 2\gamma$, $\Omega_{c0} = 0.5\gamma$, and the rest are the same as in Fig. 4.

within the central petal region. As one moves away from the center, the intensity distribution for other orders displays thin petal-shaped regions.

3. Dependence on atomic interaction length

In the following part and as depicted in Fig. 8, we present the different orders of the Fraunhofer diffraction patterns cor-

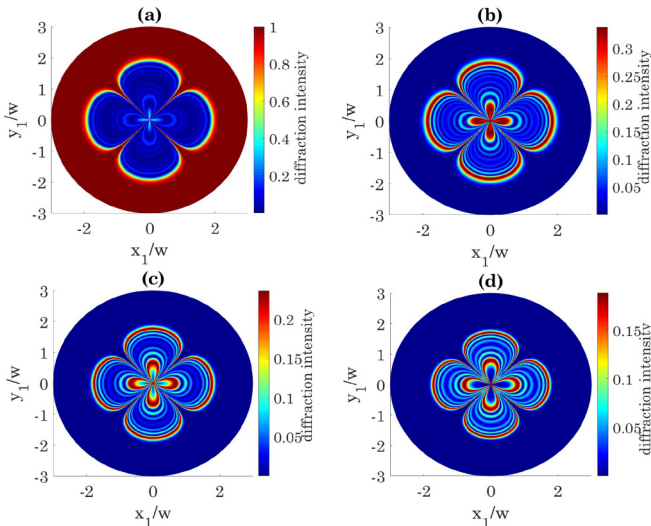


FIG. 7. Spatial dependency of the different diffraction orders versus x_1/w and y_1/w for winding number $l = 2$. Panel (a) corresponds to the zero order, (b) corresponds to the first order, (c) corresponds to the second order, and (d) corresponds to the third order. The intensity distribution exhibits petal-like patterns for different degrees of diffraction. The selected parameters are the same as in Fig. 6.

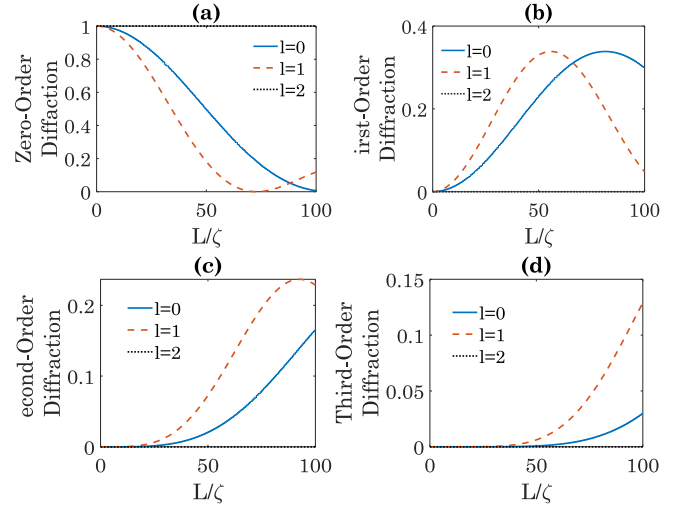


FIG. 8. Different orders of Fraunhofer diffraction as a function of the atomic interaction length L/ξ corresponds to (a) the zero order, (b) the first order, (c) the second order, and (d) the third order for $r/w = 1$, $\varphi = \pi/4$, and $\Delta_p = \Delta_c = \Delta_{LG} = 0$. It is fascinating to observe that the first- to third-order contributions are prominent at larger values of L/ξ , while they do not have any significant impact at smaller L/ξ . The selected parameters are the same as in Fig. 4.

responding to various OAM numbers relative to the atomic interaction length (L/ξ). In our analysis, we consider a composite vortex light with $r/w = 1$ and $\varphi = \pi/4$. Additionally, all the incident lights are assumed to be in resonance with their respective transitions, i.e., $\Delta_p = \Delta_c = \Delta_{LG} = 0$. For the case of $l = 0$ (solid line), all the intensity of the probe field accumulates at zero order. However, as the interaction length L increases, the zero-order intensity decreases and eventually reaches zero at $L = 100\xi$. It is worth noting that the intensity of this order can be controlled by adjusting the value of the OAM number. For $l = 1$ (dashed line), the intensity of the zero order also decreases, similar to the previous case. However, this time its intensity becomes zero at $L \simeq 70\xi$. In contrast, for $l = 2$ (denoted by a dotted line), the entire intensity of the probe field remains at the zero order, and its value does not change with varying the interaction length. This occurrence is because, for $l = 2$, the intensity of the composite vortex light becomes zero (e.g., $\Omega_{LG} = 0$), effectively converting the N -type atomic system into two independent two-level atomic systems. Under such conditions, the SW field has no effect on the Fraunhofer diffraction pattern of the probe field, resulting in intensities of the higher orders having initial zero values. As the interaction length increases, the intensity of different orders grows, and this can be controlled by adjusting the value of the OAM number of the composite vortex field. For the case of $l = 0$ (solid line), with the decrease of the zero-order intensity, most of the intensity is transferred to the first order. When $L = 100\xi$, the intensity of the zero order has vanished, and all the energy is transferred to the first, second, and third orders. However, increasing the OAM to $l = 1$ (dashed line) leads to most of the probe intensity gathering in the second and third orders.

Gratings of various types have garnered significant interest in a wide range of applications, including optical switching

[9], routing, and multibeam splitters [49], shaping biphoton spectra [50], and generating stationary light pulses [51]. Gratings with varying periods are also commonly used to measure topological charges [52,53]. These lattices enable dynamic control over the intensity and spatial distribution of diffraction patterns, making them particularly valuable in the context of multichannel optical communication and multiparticle capture applications.

Considering these diverse applications, our proposed model holds significant promise for several purposes. It can be employed for the measurement of topological charges in optical vortex light, enabling a better understanding of complex light-matter interactions. Moreover, it has the potential to be a valuable tool in optical light-shaping technologies, offering practical advantages in applications such as optical switching and the dynamic control of diffraction patterns.

V. CONCLUSION

In summary, we investigated the spatially dependent diffraction orders of electromagnetically induced grating (EIG) in a four-level N -type atomic system. To achieve this, we employed an excitation scheme that simultaneously interacted with a standing wave beam along the x direction and a composite vortex. Through the use of analytical methods for solving the integral equation of Fraunhofer diffraction, we established a direct link between the different diffraction orders and the corresponding Bessel functions of those orders. Our numerical analysis revealed that when the OAM of the

composite beam is set to zero, distinctive ring patterns emerge for the various diffraction orders. These ring-shaped regions exhibit different intensities, resulting from constructive or destructive interferences. As the winding numbers of the composite beam increase, the ring patterns undergo fascinating transformations, evolving into petal-like structures with varying sizes depending on the diffraction order. The behavior of the different orders of Fraunhofer diffraction patterns upon varying the atomic interaction length for different OAM numbers shows the distribution of the probe field energy. Taking advantage of the additional degree of freedom provided by the coupling composite optical vortex, we proposed a straightforward scheme for controlling the performance of the EIG. The direct control offered by our method makes it experimentally feasible in common atom optics setups and it holds great promise for constructing photonic devices and other elements for quantum technology applications. The ability to tailor and control EIGs using composite optical vortices opens up exciting possibilities for advancements in quantum optics and related fields.

ACKNOWLEDGMENTS

T.K. was supported by Grant No. LV-LT-TW/2023/10 Coherent Optical Control of Atomic Systems by the Ministry of Education and Science of the Republic of Latvia. H.R.H. acknowledges support from Grant No. S-LLT-22-2 Coherent Optical Control of Atomic Systems by the Lithuanian Council of Research.

-
- [1] H. Y. Ling, Y. Q. Li, and M. Xiao, Electromagnetically induced grating: Homogeneously broadened medium, *Phys. Rev. A* **57**, 1338 (1998).
 - [2] M. Mitsunaga and N. Imoto, Observation of an electromagnetically induced grating in cold sodium atoms, *Phys. Rev. A* **59**, 4773 (1999).
 - [3] G. S. Cardoso and J. W. R. Tabosa, Electromagnetically induced gratings in a degenerate open two-level system, *Phys. Rev. A* **65**, 033803 (2002).
 - [4] S. E. Harris, Electromagnetically induced transparency, *Phys. Today* **50**, 36 (1997).
 - [5] M. Fleischhauer, A. Imamoglu, and J. P. Marangos, Electromagnetically induced transparency: Optics in coherent media, *Rev. Mod. Phys.* **77**, 633 (2005).
 - [6] S. E. Harris, J. E. Field, and A. Imamoglu, Nonlinear optical processes using electromagnetically induced transparency, *Phys. Rev. Lett.* **64**, 1107 (1990).
 - [7] M. D. Lukin and A. Imamoglu, Nonlinear optics and quantum entanglement of ultraslow single photons, *Phys. Rev. Lett.* **84**, 1419 (2000).
 - [8] O. Firstenberg, M. Shuker, N. Davidson, and A. Ron, Elimination of the diffraction of arbitrary images imprinted on slow light, *Phys. Rev. Lett.* **102**, 043601 (2009).
 - [9] A. W. Brown and M. Xiao, All-optical switching and routing based on an electromagnetically induced absorption grating, *Opt. Lett.* **30**, 699 (2005).
 - [10] D. Moretti, D. Felinto, J. Tabosa, and A. Lezama, Dynamics of a stored Zeeman coherence grating in an external magnetic field, *J. Phys. B: At. Mol. Opt. Phys.* **43**, 115502 (2010).
 - [11] L. Zhao, W. Duan, and S. F. Yelin, All-optical beam control with high speed using image-induced blazed gratings in coherent media, *Phys. Rev. A* **82**, 013809 (2010).
 - [12] F. Wen, W. Wang, I. Ahmed, H. Wang, Y. Zhang, Y. Zhang, A. R. Mahesar, and M. Xiao, Two-dimensional Talbot self-imaging via electromagnetically induced lattice, *Sci. Rep.* **7**, 41790 (2017).
 - [13] P. W. Zhai, X. M. Su, and J. Y. Gao, Optical bistability in electromagnetically induced grating, *Phys. Lett. A* **289**, 27 (2001).
 - [14] Y. Q. Zhang, Z. K. Wu, M. R. Belić, H. B. Zheng, Z. G. Wang, M. Xiao, and Y. P. Zhang, Photonic Floquet topological insulators in atomic ensembles, *Laser Photon. Rev.* **9**, 331 (2015).
 - [15] Y. Zhang, C. Yuan, Y. Zhang, H. Zheng, H. Chen, C. Li, Z. Wang, and M. Xiao, Surface solitons of four-wave mixing in an electromagnetically induced lattice, *Laser Phys. Lett.* **10**, 055406 (2013).
 - [16] Y. Zhang, Z. Wang, Z. Nie, C. Li, H. Chen, K. Lu, and M. Xiao, Four-wave mixing dipole soliton in laser-induced atomic gratings, *Phys. Rev. Lett.* **106**, 093904 (2011).
 - [17] B. K. Dutta and P. K. Mahapatra, Electromagnetically induced grating in a three-level ξ -type system driven by a strong standing wave pump and weak probe fields, *J. Phys. B* **39**, 1145 (2006).
 - [18] T. Naseri and R. Sadighi-Bonabi, Electromagnetically induced phase grating via population trapping conditions in a

- microwave-driven four-level atomic system, *J. Opt. Soc. Am. B* **31**, 2879 (2014).
- [19] L. Wang, F. Zhou, P. Hu, Y. Niu, and S. Gong, Two dimensional electromagnetically induced cross-grating in a four-level tripod-type atomic system, *J. Phys. B: At. Mol. Opt. Phys.* **47**, 225501 (2014).
- [20] M. Sahrai, F. Bozorgzadeh, and H. Khoshshima, Phase control of electromagnetically induced grating in a four-level atomic system, *Opt. Quant. Electron.* **48**, 438 (2016).
- [21] Y. Hu, G. Cheng, and A. Chen, Tunneling-induced phase grating in quantum dot molecules, *Opt. Express* **28**, 29805 (2020).
- [22] M. M. Feili, A. Mortezapour, and A. A. Naemi, Phase-controlled electromagnetically induced grating in a quantum dot molecule, *Int. J. Theor. Phys.* **61**, 27 (2022).
- [23] Y. Liu, Y. Xiang, and A. A. Mohammed, Asymmetric diffraction grating via optical vortex light in a tunneling quantum dot molecule, *Laser Phys. Lett.* **19**, 095205 (2022).
- [24] S. H. Asadpour, A. Panahpour, and M. Jafari, Phase-dependent electromagnetically induced grating in a four-level quantum system near a plasmonic nanostructure, *Eur. Phys. J. Plus* **133**, 411 (2018).
- [25] S. H. Asadpour, T. Kirova, H. R. Hamed, V. Yannopapas, and E. Paspalakis, Azimuthal dependence of electromagnetically induced grating in a double V-type atomic system near a plasmonic nanostructure, *Eur. Phys. J. Plus* **138**, 246 (2023).
- [26] S. H. Asadpour, T. Kirova, J. Qian, H. R. Hamed, G. Juzeliūnas, and E. Paspalakis, Azimuthal modulation of electromagnetically induced grating using structured light, *Sci. Rep.* **11**, 20721 (2021).
- [27] L. Allen, M. J. Padgett, and M. Babiker, IV The orbital angular momentum of light, *Prog. Opt.* **39**, 291 (1999).
- [28] M. Padgett, J. Courtial, and L. Allen, Light's orbital angular momentum, *Phys. Today* **57**(5), 35 (2004).
- [29] M. Babiker, D. L. Andrews, and V. E. Lembessis, Atoms in complex twisted light, *J. Opt.* **21**, 013001 (2019).
- [30] Z. Dutton and J. Ruostekoski, Transfer and storage of vortex states in light and matter waves, *Phys. Rev. Lett.* **93**, 193602 (2004).
- [31] H. R. Hamed, J. Ruseckas, E. Paspalakis, and G. Juzeliūnas, Transfer of optical vortices in coherently prepared media, *Phys. Rev. A* **99**, 033812 (2019).
- [32] J. Ruseckas, A. Mekys, and G. Juzeliūnas, Optical vortices of slow light using a tripod scheme, *J. Opt.* **13**, 064013 (2011).
- [33] T. Wang, L. Zhao, L. Jiang, and S. F. Yelin, Diffusion-induced decoherence of stored optical vortices, *Phys. Rev. A* **77**, 043815 (2008).
- [34] R. Pugatch, M. Shuker, O. Firstenberg, A. Ron, and N. Davidson, Topological stability of stored optical vortices, *Phys. Rev. Lett.* **98**, 203601 (2007).
- [35] D. Moretti, D. Felinto, and J. W. R. Tabosa, Collapses and revivals of stored orbital angular momentum of light in a cold-atom ensemble, *Phys. Rev. A* **79**, 023825 (2009).
- [36] D. Maleev, and G. Swartzlander, Composite optical vortices, *J. Opt. Soc. Am. B* **20**, 1169 (2003).
- [37] S. M. Baumann, D. M. Kalb, L. H. MacMillan, and E. J. Galvez, Propagation dynamics of optical vortices due to Gouy phase, *Opt. Express* **17**, 9818 (2009).
- [38] H. R. Hamed, E. Paspalakis, G. Zlabys, G. Juzeliūnas, and J. Ruseckas, Complete energy conversion between light beams carrying orbital angular momentum using coherent population trapping for a coherently driven double-lambda atom-light-coupling scheme, *Phys. Rev. A* **100**, 023811 (2019).
- [39] S. H. Asadpour, H. R. Hamed, T. Kirova, and E. Paspalakis, Two-dimensional electromagnetically induced phase grating via composite vortex light, *Phys. Rev. A* **105**, 043709 (2022).
- [40] A. Wahab, M. Abbas, and B. C. Sanders, Effect of composite vortex beam on a two-dimensional gain assisted atomic grating, *New J. Phys.* **25**, 053003 (2023).
- [41] V. G. Arkhipkin, D. A. Ikonnikov, and S. A. Myslivets, Diffraction of a Laguerre-Gaussian beam in Raman interaction with a spatially periodic pump field, *Phys. Rev. A* **107**, 023519 (2023).
- [42] D. A. Ikonnikov, S. A. Myslivets, V. G. Arkhipkin, and A. M. Vyunishev, Near-field evolution of optical vortices and their spatial ordering behind a fork-shaped grating, *Photonics* **10**, 469 (2023).
- [43] S. Franke-Arnold, J. Leach, M. J. Padgett, V. E. Lembessis, D. Ellinas, A. J. Wright, J. M. Girkin, P. Öhberg, and A. S. Arnold, Optical ferris wheel for ultracold atoms, *Opt. Express* **15**, 8619 (2007).
- [44] X. He, P. Xu, J. Wang, and M. Zhan, Rotating single atoms in a ring lattice generated by a spatial light modulator, *Opt. Express* **17**, 21007 (2009).
- [45] V. E. Lembessis, A. Alqarni, S. Alshamari, A. Siddig, and O. M. Aldossary, Artificial gauge magnetic and electric fields for free two-level atoms interacting with optical ferris wheel light fields, *J. Opt. Soc. Am. B* **34**, 1122 (2017).
- [46] P. M. Blanchard, D. J. Fisher, S. C. Woods, and A. H. Greenaway, Phase-diversity wave-front sensing with a distorted diffraction grating, *Appl. Opt.* **39**, 6649 (2000).
- [47] A. S. Desyatnikov, A. A. Sukhorukov, and Y. S. Kivshar, Azimuthons: Spatially modulated vortex solitons, *Phys. Rev. Lett.* **95**, 203904 (2005).
- [48] A. Bekshaev and M. Soskin, Rotational transformations and transverse energy flow in paraxial light beams: linear azimuthons, *Opt. Lett.* **31**, 2199 (2006).
- [49] Y.-Y. Chen, Z.-Z. Liu, and R.-G. Wan, Beam splitter and router via an incoherent pump-assisted electromagnetically induced blazed grating, *Appl. Opt.* **56**, 5736 (2017).
- [50] J. Wen, Y.-H. Zhai, S. Du, and M. Xiao, Beam splitter and router via an incoherent pump-assisted electromagnetically induced blazed grating, *Phys. Rev. A* **82**, 043814 (2010).
- [51] M. Bajcsy, A. S. Zibrov, and M. D. Lukin, Stationary pulses of light in an atomic medium, *Nature (London)* **426**, 638 (2003).
- [52] K. Dai, C. Gao, L. Zhong, Q. Na, and Q. Wang, Measuring OAM states of light beams with gradually-changing-period gratings, *Opt. Lett.* **40**, 562 (2015).
- [53] S. Zheng and J. Wang, Measuring orbital angular momentum (OAM) states of vortex beams with annular gratings, *Sci. Rep.* **7**, 40781 (2017).